Article

Improving the Accuracy of Landsat 8 Land Surface Temperature in Arid Regions by MODIS Water Vapor Imagery

Fahime Arabi Aliabad [1], Mohammad Zare [1], Hamidreza Ghafarian Malamiri [2] and Ebrahim Ghaderpour [3,4,*]

1 Department of Arid Lands Management, Faculty of Natural Resources and Desert Studies, Yazd University, Yazd 8915818411, Iran; fahimearabi@stu.yazd.ac.ir (F.A.A.); mzernani@yazd.ac.ir (M.Z.)
2 Department of Geography, Yazd University, Yazd 8915818411, Iran; hrghafarian@yazd.ac.ir
3 Department of Earth Sciences & CERI Research Centre, Sapienza University of Rome, P.le. Aldo Moro, 5, 00185 Rome, Italy
4 Earth and Space Inc., Calgary, AB T3A5B1, Canada
* Correspondence: ebrahim.ghaderpour@uniroma1.it

Abstract: Land surface temperature (LST) is a significant environmental factor in many studies. LST estimation methods require various parameters, such as emissivity, temperature, atmospheric transmittance and water vapor. Uncertainty in these parameters can cause error in LST estimation. The present study shows how the moderate resolution imaging spectroradiometer (MODIS) water vapor imagery can improve the accuracy of Landsat 8 LST in different land covers of arid regions of Yazd province in Iran. For this purpose, water vapor variation is analyzed for different land covers within different seasons. Validation is performed using T-based and cross-validation methods. The image of atmospheric water vapor is estimated using the MODIS sensor, and its changes are investigated in different land covers. The bare lands and sparse vegetation show the highest and lowest accuracy levels for T-based validation, respectively. The root mean square error (RMSE) is also calculated as 0.57 °C and 1.41 °C for the improved and general split-window (SW) algorithms, respectively. The cross-validation results show that the use of the MODIS water vapor imagery in the SW algorithm leads to a reduction of about 2.2% in the area where the RMSE group is above 5 °C.

Keywords: cross-validation; Landsat; Land surface temperature; MODIS; Sentinel-2; split-window algorithm; water vapor retrieval; Yazd

1. Introduction

The land surface temperature (LST) affects the energy exchanges between the earth and atmosphere, climatic, hydrological, and environmental processes [1,2]. LST is the most important component in modeling and estimating of evapotranspiration, plants drought stress, soil moisture, fire, and geothermal hazards [3,4]. Along with the high demand for information on the spatiotemporal variations in LST, the accurate estimation of this parameter has become crucial [5]. However, it is not possible to monitor temperature on a large scale through ground-based measurements [6,7]. Therefore, remote sensing techniques are the most efficient ways of estimating the LST on regional and global scales in the lowest time and with the least cost [7]. Remote sensing-derived LST has been widely utilized for environmental monitoring, vegetation, and climate change studies [8,9].

LST estimation using satellite imagery depends on the atmospheric effects, sensor parameters, spectral range, viewing angle, and land surface characteristics, such as emissivity and geometry [10,11]. Thermal infrared radiation (TIR) is most affected by the atmospheric effects and irregular land surface emissivity [12]. Therefore, satellite imagery-based LST estimation methods require surface and atmospheric parameters, such as surface emissivity, air temperature, atmospheric transmission coefficient, and water vapor as inputs. Uncertainty in these parameters causes errors in the LST retrieval [13]. Atmospheric profile

information at the satellite transition time can be measured using radiosonde. However, radiosondes with sufficient spatial resolution and information measured at the satellite transition time are not available [14]. In addition, due to the spatial-temporal variations in the atmospheric parameters, such as water vapor and air temperature, the use of ground radiosonde being distant from the study area or away from the satellite transition time may lead to an error in estimating LST [15].

Knowing the atmospheric water vapor (AWV) improves the accuracy of estimating land surface parameters in remote sensing [16,17]. Over the past two decades, various methods have been developed for estimating AWV using remote sensing [18,19]. Depending on the used wavelength, these methods are divided into three categories, including the near-infrared methods [20,21], inactive microwave [7,22], and thermal infrared [23,24]. The near-infrared approach is more practical than other ones. This method relies on reducing water vapor in near-infrared radiation. In this technique, the amount of AWV is estimated using the ratio between the bands affected by the water vapor absorption and those of an ineffective atmospheric window [25].

Many researchers have studied the importance of water vapor parameters in accurately estimating LST using remote sensing [26,27]. Wang et al. reported that the error in the amount of AWV has the most significant effect on reducing the accuracy of LST estimation [28]. Cristobal et al. presented an improved method for estimating LST [29]. Their results showed that using the air temperature parameter and water vapor amount increases the accuracy of LST estimation. During recent years, researchers have estimated the amount of water vapor using the satellite images [30–32]. Albert et al. compared the amount of AWV obtained via moderate resolution imaging spectroradiometer (MODIS) images and radiosonde's data and estimated the root mean square error (RMSE) to be 2 kg/m^2 [33]. Moradizadeh et al. estimated the water vapor using the MODIS sensor's images and validated it with an atmospheric infrared sounder (AIRS) product [19]. The results of MODIS water vapor validation indicated an error of at least 9%. Varamesh et al. estimated MODIS water vapor images and illustrated that bare lands and rangelands have the lowest water vapor levels [34]. Vaquero-Martínez et al. proved that the seasonal cycle of the solar zenith angle has changed the AWV in different seasons [35].

The current study aims to evaluate the effect of MODIS water vapor on improving the accuracy of Landsat 8 LST images for arid regions. In addition, the changing rate of water vapor in different land covers is examined. The results of this research can be useful for obtaining information on the LST with higher accuracy because the accuracy of LST estimation has a fundamental role in many studies, such as determining the water stress of plants using evaporation and transpiration, energy balance modeling, and estimating soil depth temperature.

2. Materials and Methods

2.1. Study Area

The present research was conducted in the Yazd Ardakan plain and a desert region with a hot and dry climate. In this area, in addition to very little precipitation (60 mm per year), the air temperature is very high, so that the absolute maximum temperature is 47 °C, and the temperature fluctuations are very large during the night and day, winter and summer. Therefore, this region was chosen for research due to its special climatic conditions and high temperature. Its geographical location is 53°23′48″ to 54°50′11″ east longitude and 31°18′50″ to 32°20′00″ north latitude. This region is mostly covered by flat and plain lands, but it also includes mountain (Figure 1).

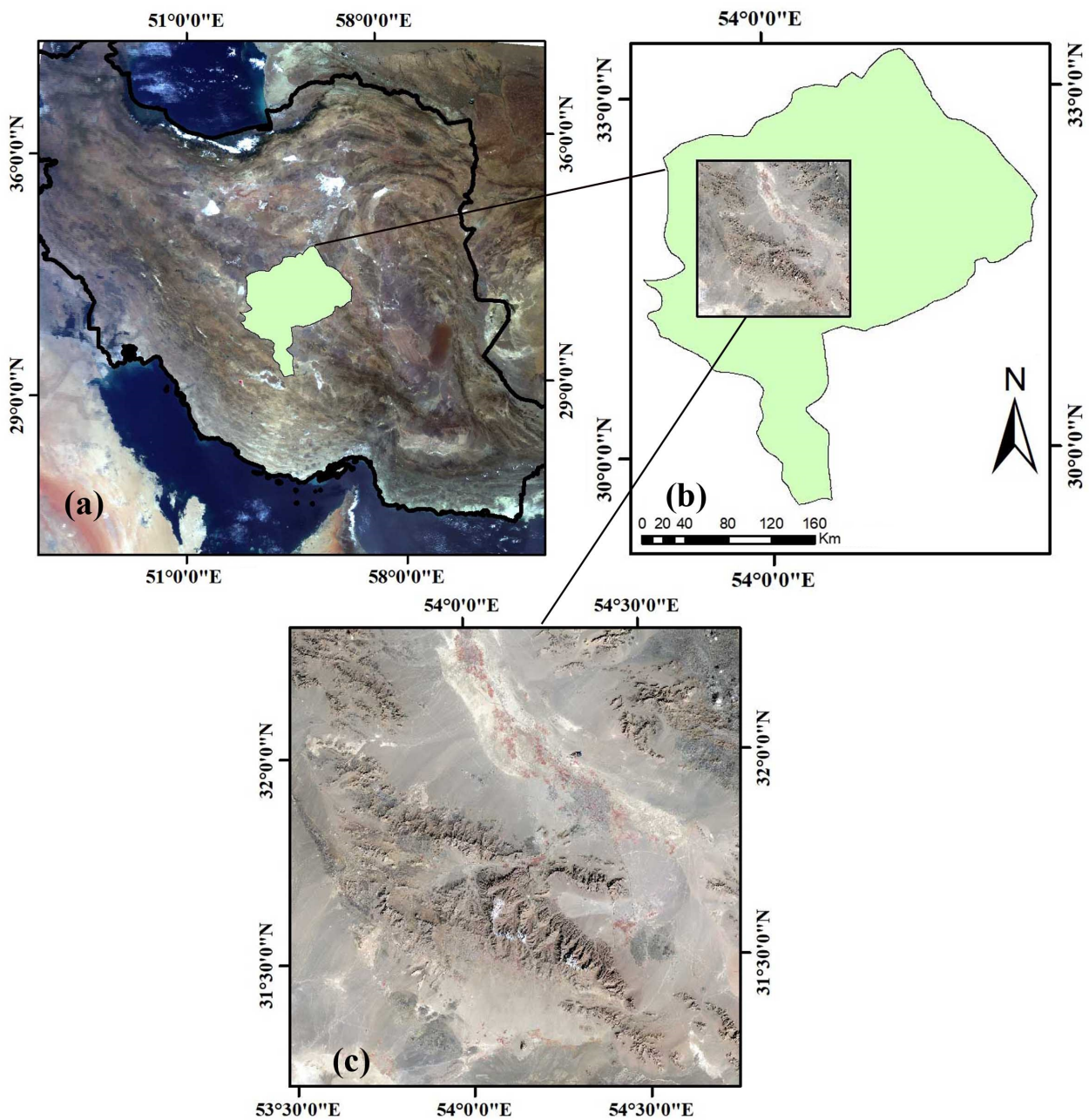**Figure 1.** (**a**) The location of Yazd province in Iran, (**b**) the location of the study area in Yazd province, and (**c**) the false color composition image of the study area using Landsat 8.

2.2. Datasets and preprocessings

2.2.1. Satellite Data

In the present study, 50 images of Landsat 8 in the period 2018–2020 were used to estimate LST. The Landsat 8 satellite carries an operational land imager (OLI) and thermal infrared sensor (TIRS). Landsat 8 includes nine spectral bands with a spatial resolution of 30 m for bands 1 to 7 and 9, two thermal bands (for 10 and 11) with a spatial resolution of 100 m and eight panchromatic bands with a resolution of 15 m [36]. The main difference between the new TIRS sensor on the Landsat 8 satellite and the previous TM and ETM ones is the presence of two TIR bands in the 10.8–12 μm atmospheric window. This has led to the use of the split-window (SW) algorithm for calculating LST [37].

To estimate AWV, bands 2, 17, 18, and 19 of the MODIS radiance image, called MOD021, were used with a spatial resolution of 1 km. The MODIS is a key instrument

aboard both the NASA's Terra and Aqua satellites, viewing the regions poleward of 60° as many as 10–14 times a day and acquiring data in 36 spectral channels in the visible, near infrared (NIR), and thermal infrared bands [38]. In this study, the MODIS-LST product, called MOD11A1, was employed for cross-validation. The MODIS sensor has created the ability to obtain LST images with a resolution of 1 km with a sequence of four times a day and night [39]. The MODIS-LST, which exists under the names MOD11 and MYD11, is estimated using the split window algorithm. This algorithm is highly accurate and uses two thermal bands 31 (10.78–11.28 μm) and 32 (11.77–12.27 μm). The accuracy of MODIS-LST has been checked using validation stations in many studies, and the results have shown that for temperatures between 10 °C and 50 °C and AWV between 0.4 and 4 cm/km, this product can measure the temperature of the Earth's surface with an error of less than 1 °C [40–43].

The Sentinel-2 satellite images were employed to prepare the land cover map. Having high spectral and spatial resolutions, this satellite has a high potential for preparing land cover maps [44]. Sentinel-2 was designed by the European Space Agency (ESA) and launched in 2015. This satellite carries the multi-spectral instrument (MSI) sensor, which covers the entire earth every 5 days within 13 spectral bands of 10–60 m spatial resolution [45]. The general specifications of the images used in this research are listed in Table 1.

Table 1. Specifications of satellite images used in the present study.

Satellite	Bands	Wavelength (μm)	Resolution (m)
Landsat 8	Band 4—Red	0.64–0.67	30
Landsat 8	Band 5—Near Infrared (NIR)	0.85–0.88	30
Landsat 8	Band 10—Thermal Infrared	10.60–11.19	100
Landsat 8	Band 11—Thermal Infrared (TIRS) 2	11.50–12.51	100
Sentinel-2A	Band 2—Blue	0.458–0.523	10
Sentinel-2A	Band 3—Green	0.543–0.578	10
Sentinel-2A	Band 4—Red	0.650–0.680	10
Sentinel-2A	Band 8—Near Infrared (NIR)	0.785–0.899	10
MOD021	Band 2—Land/Cloud/Aerosols	0.876–0.841	250
MOD021	Band 17—Water Vapor	0.920–0.890	1000
MOD021	Band 18—Water Vapor	0.941–0.931	1000
MOD021	Band 19—Water Vapor	0.965–0.915	1000
MOD11	Land Surface Temperature (LST)		1000

2.2.2. In Situ Data

To perform the LST ground validation, the temperature was measured using thermometers during the satellite transition times on 16 May 2020 and 14 April 2020. Due to the vastness of the study area, including different land covers, it has been attempted to conduct sampling for all land covers. Conducting the uncontrolled classification on the Sentinel satellite's images, the maximum land cover separation was performed. Then, the homogeneous areas were separated, and areas with net pixels were selected for validation. A total of 30 validation points were chosen to conduct the ground measurement of LST.

In the present study, AWV was evaluated using MODIS imagery, and its effect was investigated using the SW algorithm on the accuracy of LST obtained via this satellite. The LST accuracy was assessed using the ground and cross-validation methods. For the cross-validation method, MODIS-LST images were used, and ground temperature (GT) manually measured at the validation points was used to conduct the ground validation. The land cover map was prepared using the Sentinel-2 images, and the maximum probability method was employed to examine the variation rate of AWV and LST estimation error at different land covers. The schematic of the research steps is shown in Figure 2.
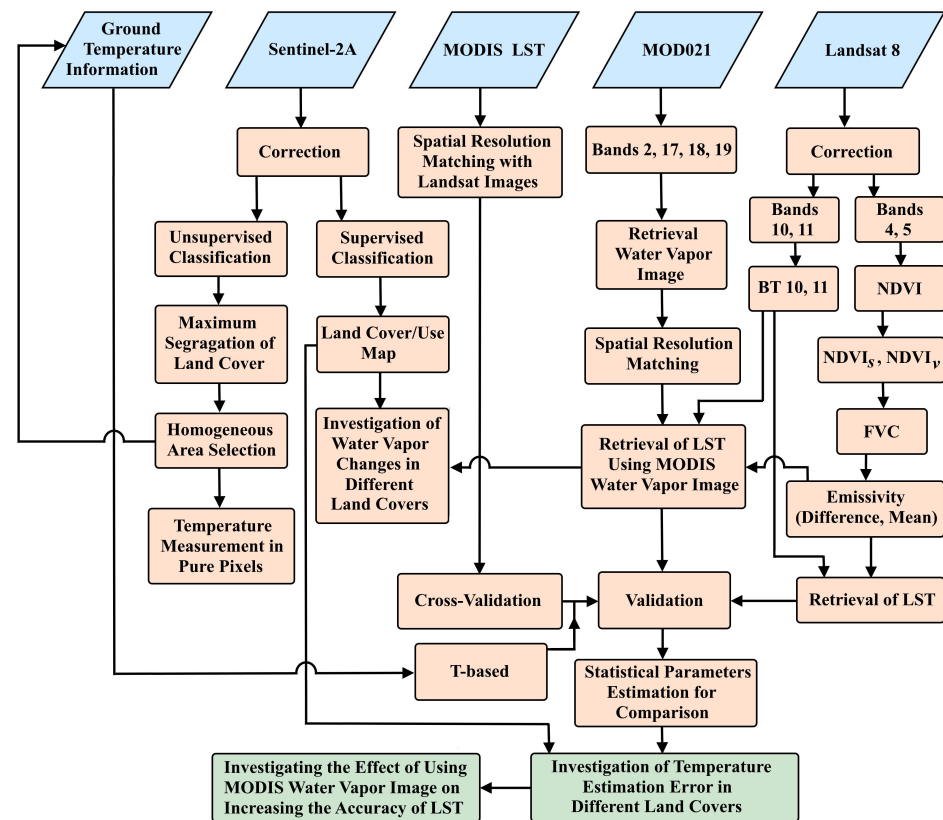
Figure 2. Flowchart of this research.

2.3. Methodology

The difference between the previous LST estimation method using the split window algorithm and the proposed method herein is that the component of the atmospheric water vapor column is considered a constant number in the previous method, but the atmospheric water vapor image of the MODIS sensor is used in the proposed method. The following parts describe these techniques in more detail.

2.3.1. Land Surface Temperature Estimation

There are many methods to retrieve LST by satellite images, such as via SW [46], mono-window [47], and single-channel algorithms [48]. The SW algorithm is a multi-channel one which, in addition to being widely applicable, is more accurate than other methods [49]. The advantage of the SW method is the use of the absorption difference between two thermal bands in estimating the temperature and automatic correction of the atmospheric effects [50,51]. The SW methods are generally divided into two groups of linear [47,52] and nonlinear [53,54]. The linear (nonlinear) SW method expresses LST as a linear (nonlinear) combination of the brightness temperature (BT) for two TIR bands (T_i and T_j). The general equation for the linear SW algorithm is given as

$$\text{LST} = A_0 + A_1 T_i + A_2(T_i - T_j), \tag{1}$$

while that of the nonlinear one is in the form

$$\text{LST} = A_0 + A_1 T_i + A_2(T_i - T_j) + A_2(T_i - T_j)^2, \tag{2}$$

where A_k ($k = 0, 1, 2, 3$) are the SW coefficients and are mainly dependent on the land surface emissivity (LSE), AWV, and viewing zenith angle (VZA) [5]. During recent decades, various SW algorithms have been proposed, which differ in determining the parameters. In the present study, the SW method presented by Jimenez-Muñoz et al. [55] was employed,

which has been more accurate than other ones according to the results of the conducted studies [56].

To estimate LST using Landsat 8 images, it is necessary to first convert digital values into spectral energy in the sensor, and in this way, the spectral energy in the sensor is estimated for two thermal bands. In addition to this component, two constant parameters K_1 and K_2 are needed to calculate the BT in Landsat 8 thermal bands. These two coefficients are calculated by the effective wavelength received from the sensor. The K_1 coefficient values in bands 10 and 11 are 774.89 and 480.89 (W/ (m^2 sr µm)), respectively, and the K_2 coefficient values are 1321.08 and 1201.14, respectively (in Kelvin). Emissivity estimation is needed to estimate LST. Emissivity is the measure of an object's ability to emit infrared energy [57]. In general, there are two methods for extracting LSE: first calculating emissivity through the normalized difference vegetation index (NDVI), and second calculating emissivity using the land cover map [58]. In the current study, the first approach was employed for the LSE estimation.

To estimate emissivity using the vegetation index, it is necessary to separate the soil and plant's NDVI indices. These indices have been evaluated through thresholding. Therefore, in areas where NDVI is more than 0.2, it indicates the presence of vegetation, so it was considered as $NDVI_v$ and lower values were placed in $NDVI_s$ category. The fractional vegetation cover (FVC) index was estimated, and then LSE was computed to estimate LST, see [59–61] for the mathematical formulas of spectral radiation, BT, NDVI, FVC, LSE, and LST, e.g., see Equations (1)–(6) in [61]. In this research, the amount of water vapor has been estimated using the MODIS images.

2.3.2. Estimation of Water Vapor

The amount of AWV refers to the compression of total water vapor of the atmospheric column and measurement of its height per unit area, expressed in g/cm^2 or kg/m^2 [62,63]. The AWV can be estimated using the near-infrared bands within the range of 0.88–0.97 µm, which are the main absorbers of AWV, and their comparison with non-sensitive water vapor bands from 0.865 ± 0.04 µm [20]. The water vapor estimation algorithm using MODIS images was first proposed by Sobrino et al. [64]. The MODIS bands 17–19 are located in the water vapor-sensitive area, while band 2 is located at insensitive wavelengths. Band 2 was used to eliminate the reflectance of the land surface cover. The ratio between water vapor-sensitive area bands (bands 17–19), and band 2 is estimated by

$$G_k = \frac{L_k}{L_2}, \tag{3}$$

where $k = 17, 18, 19$ and L_k is the radiance of bands 2, 17, 18, 19 of the MODIS sensor. Then, the water vapor associated with each of these bands was estimated using simulated coefficients by MODTRAN 3.5 and six standard atmospheric columns and also for ten types of land covers including fresh snow, forest, farm, desert, ocean, cloud, old grassland, rotten grassland, maple leaves, and burnt grass [64]. Suppose that W_{17}, W_{18}, and W_{19} are the water vapor values associated with MODIS bands 17, 18, and 19, respectively. Then

$$
\begin{aligned}
W_{17} &= 26.314 - 54.434 G_{17} + 28.449 G_{17}^2, \\
W_{18} &= 5.012 - 23.017 G_{18} + 27.884 G_{18}^2, \\
W_{19} &= 9.446 - 26.887 G_{19} + 19.914 G_{19}^2.
\end{aligned}
\tag{4}
$$

The AWV has different absorption coefficients in bands 17, 18, and 19 of the MODIS sensor. Under certain weather conditions, the amount of water vapor obtained via the three bands varies. The average amount of water vapor can be obtained by

$$W = f_{17}W_{17} + f_{18}W_{18} + f_{19}W_{19}, \tag{5}$$

where coefficients f_{17}, f_{18}, and f_{19} are calculated by

$$f_k = \eta_k \Big/ \sum \eta_k, \tag{6}$$

where $\eta_k = |\Delta\tau_k|/|\Delta W|$, ΔW is the maximum value minus minimum value of the water vapor content from the six standard atmospheres, and $\Delta\tau_k$ is the difference between the maximum and the minimum transmissivities for the water vapor amount calculated in channel k, for k in $\{17, 18, 19\}$ [21]. The correlation among water vapor content and transmissivity explains this relation. The estimated values for η_{17}, η_{18}, η_{19}, f_{17}, f_{18}, and f_{19} are 0.062, 0.147, 0.115, 0.191, 0.454, and 0.355, respectively [64]. This is a simple model for calculating the total water vapor from MODIS imagery directly from radiance measurements.

2.3.3. Land Cover Classification

To investigate the variation rate of AWV and estimation error of LST in different land covers, a land cover map of the study area was prepared. For this purpose, the Sentinel-2 images with a 10 m resolution were used along with the maximum likelihood method. The maximum likelihood algorithm is one of the most well-known and widely used information classification methods among the controlled classification ones [65]. In this method, the pixel is placed in the class that has the highest probability [66].

2.3.4. Validation of Land Surface Temperature

Assessing the LST retrieval accuracy is one of the most important challenges in remote sensing [7,67]. This is mainly since LST is a complex variable that is influenced by many factors and changes rapidly over time and space [68,69]. There are three methods for validating LST obtained via satellite data, including validation using the GT data (T-based), radiance-based (R-based), and cross-validation methods [15]. The ground validation method directly compares the satellite-based LST with the one measured at the time when the satellite passes over the study area [70,71]. The R-based technique is a method of simulating and comparing the estimated temperature achieved via satellite data with the results of the radiation transmission model that requires accurate knowledge of LSE, surface conditions and atmospheric profiles at the sensor transition time [72,73]. Also, the cross-validation method considers a highly validated LST product as a reference and compares the estimated LST with it [74,75]. In the present study, the two methods of ground and cross-validation are applied. In the cross-validation method, MODIS-LST images are used as a basis, while the ground validation approach uses the ground data extracted from 22 ground points.

To evaluate the accuracy of the improved LST using the water vapor image and compare it with the MODIS-LST products and ground data, the mean absolute differences (MAD), RMSE, and the standard deviation (SD) of differences were used according to the following equations [76]:

$$\mathrm{MAD} = \sum_{k=1}^{N} \left| \mathrm{LST}_{A_k} - \mathrm{LST}_{F_k} \right| \Big/ N \tag{7}$$

$$\mathrm{RMSE} = \sqrt{ \sum_{k=1}^{N} (\mathrm{LST}_{A_k} - \mathrm{LST}_{F_k})^2 \Big/ N } \tag{8}$$

$$\mathrm{SD}_{\mathrm{LST}} = \sqrt{ \sum_{k=1}^{N} \left[(\mathrm{LST}_{A_k} - \mathrm{LST}_{F_k}) - \mathrm{MD}_{\mathrm{LST}} \right]^2 \Big/ (N-1) } \tag{9}$$

In these equations, LST_{A_k} and LST_{F_k} are LST obtained via MODIS or ground validation points and Landsat 8, respectively, and N stands for the number of selected validation pixels or points. In addition, $\mathrm{MD}_{\mathrm{LST}}$ is the mean of differences.

3. Results

3.1. Investigating Atmospheric Water Vapor Changes in Different Land Covers and in Time Series

To prepare the land cover map, six classes were identified in the study area, namely agricultural, residential areas, mountain and rocky lands, rangelands, bare lands, and sand dunes. Inheritance and field data were collected. The training samples were then collected from the area using aerial photographs, Google Earth images, and field observations. Using the image characteristics, land covers were determined within the study area. After separating the classes, the controlled classification of the maximum likelihood was performed. The kappa and overall accuracy coefficients were estimated at 0.86 and 0.98, respectively, indicating the acceptable accuracy of this classification method. According to the results, 2.61, 3.53, 30.32, 51.54, 2.78, and 9.19% of the study area in 2019 was composed of agricultural lands, urban areas, mountain, rangelands, bare lands, and sand dunes, respectively.

To investigate the amount of AWV in different land covers, the corresponding values were estimated using MODIS images during the timeframe of 2018-2019. Then, the values of mean maximum, mean minimum, mean, variation range, and standard deviation were examined for each land cover in one year (Table 2). Moreover, the mean AWV values corresponding to the bare lands, rangelands, sand dunes, residential areas, agricultural and mountainous lands were reported to be 0.18, 0.18, 0.19, 0.20, 0.20, and 0.21 g/cm^2, respectively. The maximum and minimum AWV values are dedicated to the mountain and bare lands, respectively. The range of changes in the water vapor column in dry areas is small, but this small amount is effective in the accuracy of LST estimation.

Table 2. Comparison of minimum (Min), maximum (Max), range, mean, and standard deviation (SD) of AWV in different land covers. The unit of all the values is g/cm^2.

Land Cover	Min	Max	Range	Mean	SD
Agriculture	0.063	0.393	0.330	0.196	0.061
Residential	0.106	0.397	0.291	0.201	0.047
Mountain	0.106	0.351	0.245	0.211	0.031
Rangelands	0.106	0.398	0.292	0.182	0.046
Bare lands	0.095	0.398	0.303	0.179	0.059
Sand dunes	0.106	0.395	0.289	0.188	0.045

To examine the water vapor changes for different land covers, three transects were drawn on the water vapor and land cover images (Figure 3). A comparison of these values indicates the difference between the water vapor amounts associated with different land covers and indicates the importance of estimating this component and using its image instead of a fixed value.

3.2. Validation of the Improved LST Method and Its Comparison with the Split Window Method

The difference between the improved LST index using MODIS water vapor images and the temperature resulting from the general SW algorithm was investigated within one year. Also, the mean value of this difference for various land covers was estimated as well. The results indicated that in all seasons of the year, the highest to the lowest LST differences between these two indicators are associated with mountain, residential, agricultural, sand dunes, rangelands, and bare lands, respectively (Figure 4). Hence, a greater difference is observable between the improved LST and general indicators in land cover having the highest amount of water vapor.
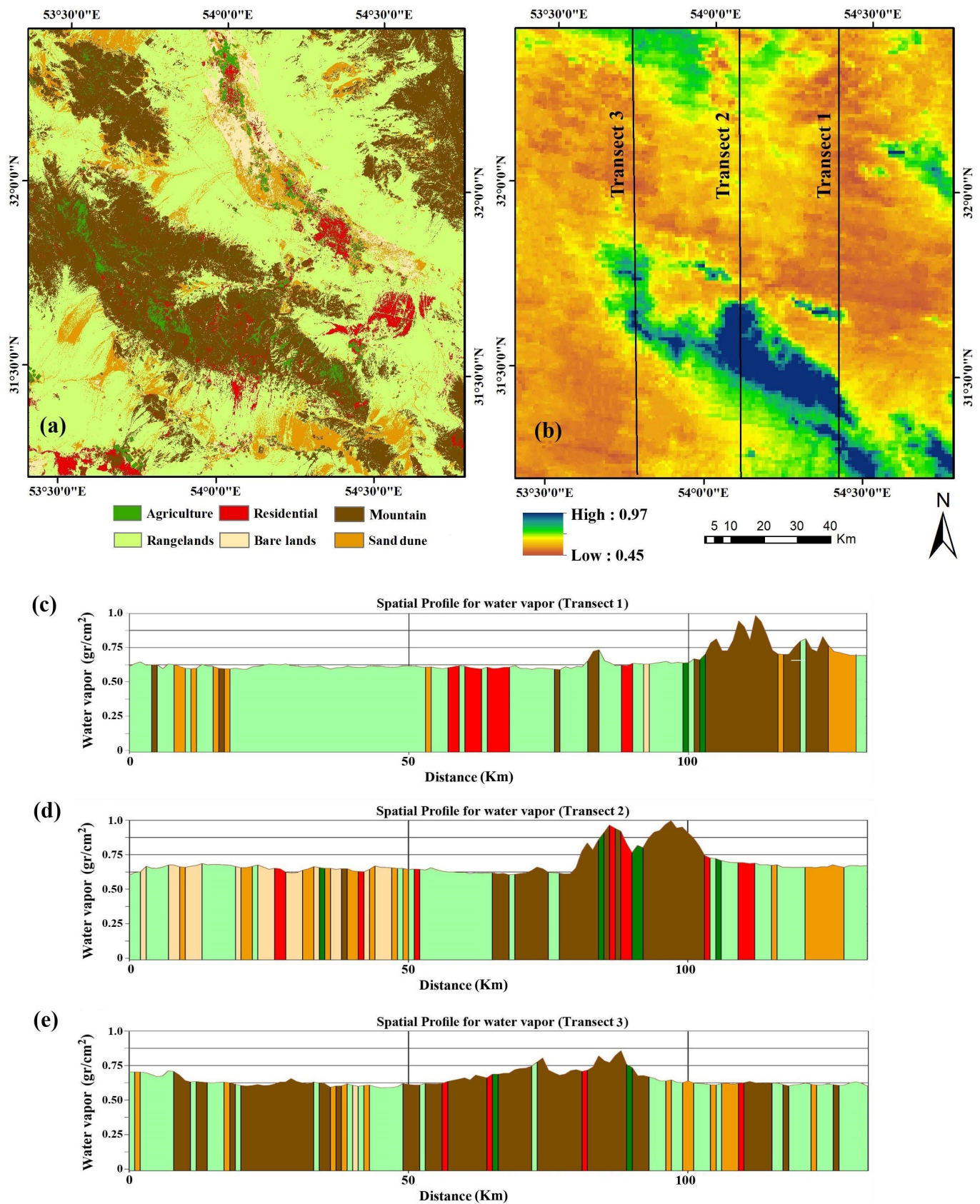
Figure 3. (**a**) Land cover map by maximum likelihood method; (**b**) atmospheric water vapor image estimated with MODIS; (**c–e**) transects 1, 2, and 3, respectively. The colors in panels (**c–e**) are the same as the colors explained in panel (**a**).

In the present study, GT measured by the thermometer during the Landsat 8 satellite passing times were used for the ground validation. Considering that each pixel in the MODIS-LST image has a spatial resolution of one kilometer, ground validation and temperature measurements with a thermometer are challenging; LST is very variable and areas that consist of one type of land cover and have completely homogeneous coverage should be used for validation. Since the study has an arid and desert climate, clay soils with no vegetation, desert pavements with uniform gravel cover, and sand dunes are suitable places for ground validation by creating net pixels. In this study, it has been attempted to use points for ground validation with homogeneous cover and has created net pixels. For this reason, Sentinel-2A images were first classified in an uncontrolled manner in 10 classes to maximize the land cover segregation. Due to the vastness of the study area, the lack of quick access to points with net pixels, land cover diversity, and time limitation due to rapid temperature changes per unit time, it was impossible to measure temperature in great point numbers. The GT was measured at 30 points in areas with homogeneous cover, and attempts have been made to collect samples in different land covers, such as bare lands, sand dunes, rangelands, desert pavements, and rocky lands (Figure 5).
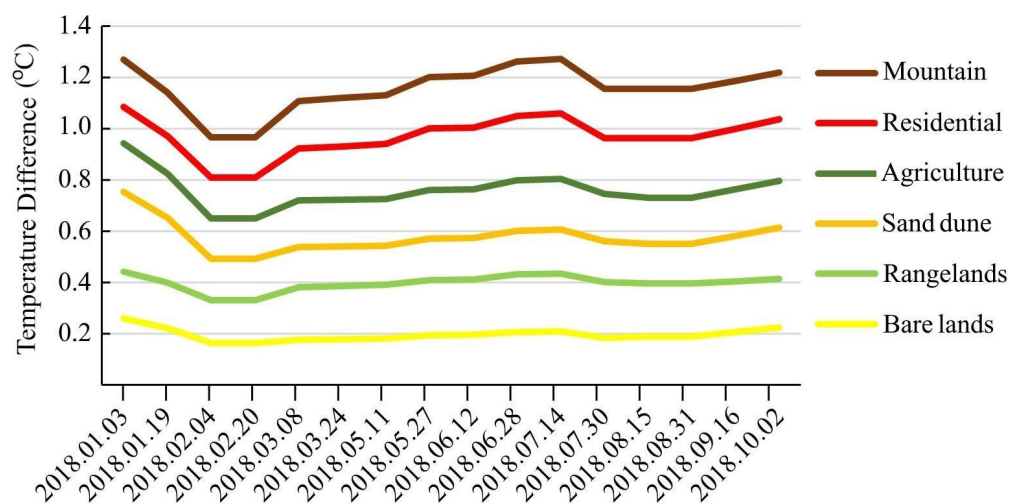

Figure 4. Changes in the differences between the improved LST and the general LST index in a year.

Note that homogeneous coverage means areas that have uniform land coverage at least in the pixel dimensions of MODIS-LST imagery. In dry areas, lands with homogeneous coverage are more accessible than other areas. Bare lands and sand dunes/Hamada that had completely uniform coverage and no plants were selected as the most reliable covers for ground validation. The GT measured at eight points in sparse vegetation areas and pistachio trees showed the highest error for validation. This was mainly due to the coarse spatial resolution of MODIS data and significant variation in temperature around those points (on the vegetation vs. nearby soil). Therefore, those eight points were excluded from the ground validation analysis. In Figure 5, two photos of LST measurements in vegetation are shown to demonstrate the extreme temperature difference in different land covers. The satellite-based LST were directly compared with the ground measurements at the same time as the satellite passed. Due to the problem of matching ground-based LST measurements with satellite-based LST pixel values, the T-based method is limited to flat and homogeneous surfaces including water, ice, snow, sand, fields, and agricultural lands. In should be noted that acquiring land-based LST measurements is a complex and difficult task due to the difference in survey scales by satellite pixels (several square kilometers) and ground sensors (several square meters).
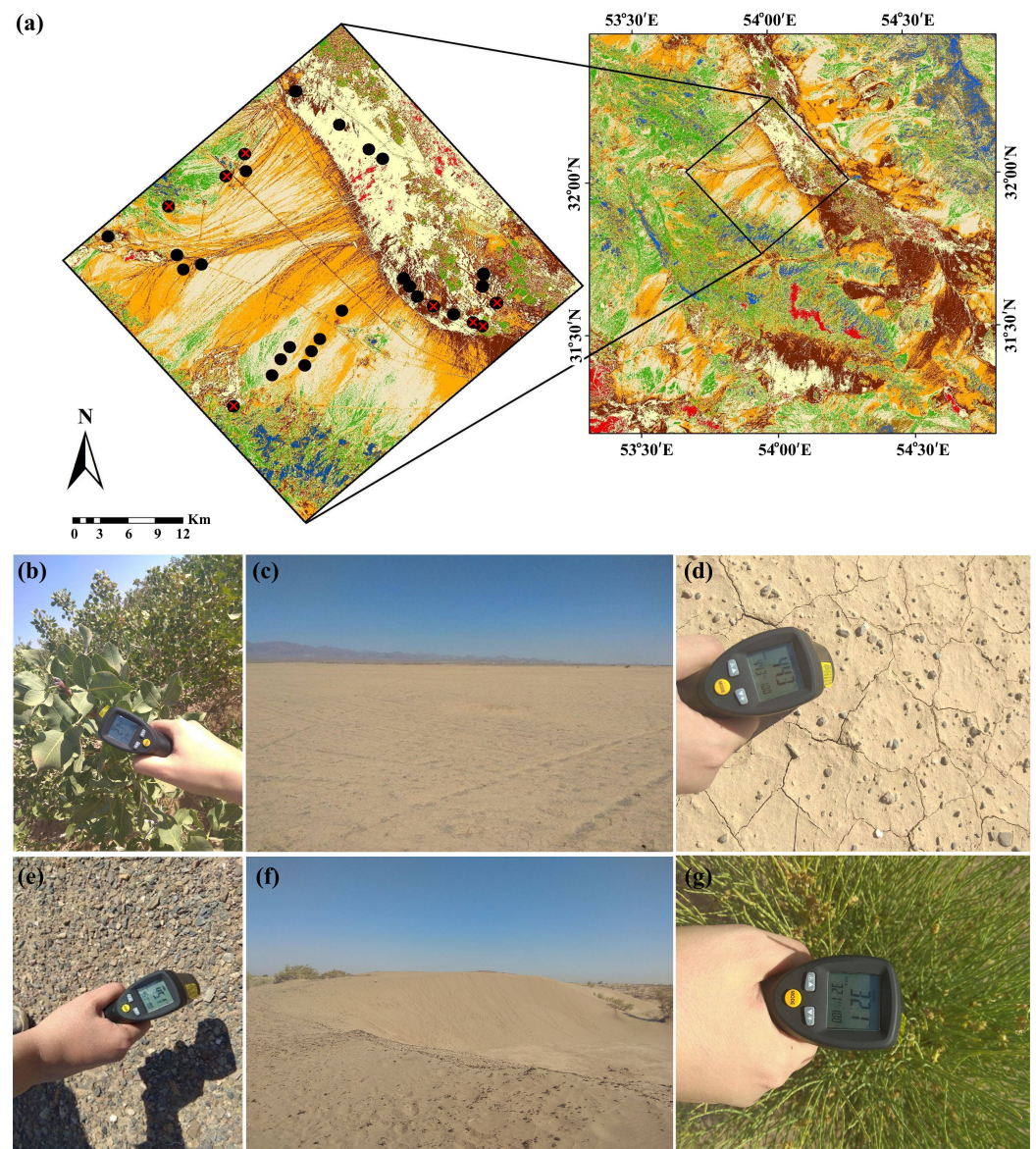
Figure 5. (**a**) The location of the ground sampling points on the map classified by unsupervised method, and temperature measurement on (**b**) trees, (**c**) bare lands, (**d**) clay lands, (**e**) desert pavements, (**f**) sand dunes, (**g**) pasture. The eight points highlighted by red cross on the top left map were located in sparse vegetation areas and were excluded from further analysis.

The GT measured by the thermometer was compared with the temperature of the corresponding points in the LST images obtained from the general SW method and the improved one using the MODIS water vapor image. The land covers and sampling time of the points are shown in Table 3. The highest temperature estimation accuracy was observed in the areas with completely homogeneous cover, such as bare lands, while areas with sparse tree or plant vegetation showed the most differences between the measured GT and the one acquired from satellites, excluded herein as shown in Figure 5.

Table 3. Land surface temperature in the improved split-window method (Improved LST), general split-window method (LST), and ground temperature (GT) at ground validation points.

Number	Land Cover	Time	Improved LST (°C)	LST (°C)	GT (°C)
1	Bare lands	9:27	42.71	44.27	42.50
2	Bare lands	9:30	43.16	41.90	43.07
3	Bare lands	9:35	42.54	41.03	42.71
4	Bare lands	9:38	41.73	43.10	42.12
5	Bare lands	9:40	43.17	41.88	42.92
6	Bare lands	9:42	42.65	41.29	42.34
7	Bare lands	9:45	40.69	41.63	39.50
8	Bare lands	9:50	42.57	43.43	42.22
9	Bare lands	9:55	42.88	41.67	42.39
10	Bare lands	9:57	41.96	40.04	42.11
11	Bare lands	10:00	42.37	41.70	42.00
12	Poor rangelands	10:08	39.78	40.25	39.56
13	Poor rangelands	10:10	39.66	40.12	39.33
14	Poor rangelands	10:12	40.90	42.14	41.21
15	Hamada	10:15	43.32	41.60	43.02
16	Hamada	10:18	43.68	42.34	43.48
17	Hamada	10:20	42.98	41.74	42.53
18	Hamada	10:22	41.50	40.78	40.65
20	Poor rangelands with Hamada	10:25	39.34	38.44	40.09
21	Poor rangelands with Hamada	10:28	38.52	37.40	40.1
22	Poor rangelands with Hamada	10:30	38.77	37.00	39.21

Furthermore, the statistical parameters of the mean absolute differences, the standard deviation of the differences, and RMSE values between the measured ground temperature and the estimated temperature using the general SW algorithm and the improved one by the MODIS sensor's water vapor image have been evaluated. According to the values listed in Table 3, the RMSE values associated with the improved method and general SW algorithm have been estimated as 1.41 °C and 0.57 °C, respectively (Table 4). It is clear that the RMSE index is a better audit than the correlation coefficient and has a higher sensitivity compared to the other statistical coefficients. Therefore, when the correlation coefficient in the method is the same, RMSE can be used to choose the better method. Therefore, the use of the MODIS sensor's water vapor image has slightly improved the accuracy of the LST estimation.

Table 4. Comparison of statistical coefficients obtained from T-based validation (°C).

Index	MAD (°C)	RMSE (°C)	SD (°C)
LST	1.26	1.41	1.81
LST Improved	0.44	0.57	1.61

For cross-validation, 50 LST images estimated using Landsat 8 were compared with the MODIS-LST product. But a problem that always exists in satellite images, especially LST images, is the presence of missing data due to clouds, dust storms (which are very common in dry areas), sensor defects, and others [7]. Missing data and outliers were removed from both MODIS and Landsat images. By comparing the temperature values in the Landsat images with the MODIS product, the RMSE image was estimated. Figure 6 shows the error rate for each point of the study area. A comparison of the percentage area associated with the general and improved SW algorithms indicates a good improvement in LST estimation. Particularly, Table 5 shows the use of the MODIS water vapor image in the improved SW algorithm has reduced the area associated with the RMSE group of above 5 °C and has led to a reduction in its area by 2.2%.

Table 5. Percentage areas associated with the general and improved SW algorithms for the RMSE groups shown in Figure 6.

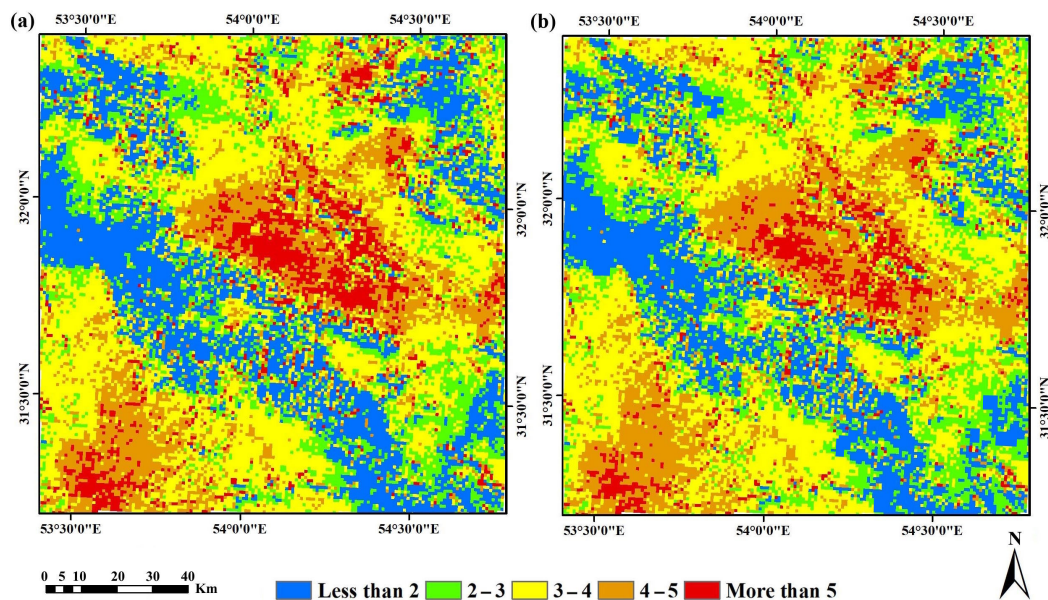| Index	2>	2–3	3–4	4–5	5<
LST	21.93	17.40	33.91	17.68	9.09
LST Improved	21.55	17.26	33.70	20.60	6.89

Figure 6. RMSE obtained from the cross-validation method: (**a**) general spilt-window method, and (**b**) improved split-window method by MODIS water vapor image.

4. Discussion

MODIS-LST has been evaluated in different climates and validation institutes, and many studies have found the accuracy of this product to be better than 1 K [77,78]. Thus, the MODIS-LST product was employed as a valid database for cross-validation of Landsat 8 LST [75]. For LST validation, using cross-validation has advantages compared to T-based measurements because this method can be used in all land covers and there is no need to find pure pixels and completely homogeneous cover areas. Therefore, the cross-validation method is applicable in areas, such as the arid region studied herein, where LST is not measured in meteorological stations and there is no database of temperature.

In the present research, the Sentinel-2A imagery were utilized only to prepare land cover maps and identify lands with homogeneous coverage because these images with a resolution of 10 m had fewer mixed-pixel issues. Sentinel-2A images were also used to select ground sampling points, and these images were classified as unsupervised. In these images, the areas that showed homogeneous coverage with the area of several Landsat 8 pixels were selected for measuring LST. The Landsat 8 image was not used for classification as it was intended to separate pure pixels as much as possible and to not use mixed pixels for temperature-based validation. Therefore, there was no need to unify the spatial resolutions of Landsat 8 and Sentinel-2 imagery.

There are some limitations in temperature-based validation. The LST changes drastically per unit of time and space. For ground validation, it is necessary to measure LST using a thermometer in areas that have homogeneous coverage and are far from the road due to the creation of mixed pixels during the passage of the satellite, so these limitations reduce the number of points. However, to improve the accuracy of validation, points with homogeneous coverage were chosen for cross-validation because measuring LST using a thermometer is performed at one point, but LST estimated by the Landsat 8 satellite shows the temperature at 100 m. Therefore, points should be selected for land validation that

have a completely uniform land cover up to a radius of at least 100 m. In addition, at each ground sampling point, the temperature was measured several times at close distances and the average was used for validation.

Utilizing the MODIS water vapor imagery with resolution of 1 km in estimating LST using Landsat 8 imagery, the final water vapor imagery reached a resolution of 100 m. In the usual method of estimating LST using Landsat 8 imagery, a constant number is used for the amount of atmospheric water vapor column, which is 0.013. However, in the proposed method, an image of the atmospheric water vapor column was estimated via MODIS sensor imagery and replaced with a fixed number. This is because it is generally inappropriate to use a fixed number for the atmospheric water vapor column component that changes throughout the year and for different land covers.

In cross-validation—an optimal method in hot and dry conditions like this study area—many areas are not accessible for ground validation. In the cross-validation, the MODIS-LST results were used. The MODIS images have been validated in many studies and their accuracy has been proven. For validation purposes, LST images estimated using the Landsat 8 satellite were converted to the resolution of MODIS images to enable comparison. Though the spatial resolution of MODIS imagery is lower than Landsat 8 imagery, it is the only available and reliable data for cross-validation, especially for arid regions where there is no meteorological station to measure temperature. Therefore, the use of the cross-validation method with MODIS images is considered an effective way to evaluate different methods of temperature estimation. It is also worthwhile to mention that the European Organization for the Exploitation of Meteorological Satellites (EUMETSAT) acquire LST data with a high temporal resolution (15 min); however, their spatial resolution is much lower (3 km nadir resolution) than Landsat, and so they were not employed in this study [79,80].

Improving the accuracy of LST even to a small amount has a great impact on the accuracy of estimating components, such as evapotranspiration and determination of plant stress. Therefore, investigating different methods for improving the accuracy of LST is very important. In several studies performed by other researchers, the LST accuracy has changed to the same extent as presented in this research [13,81,82].

Like the present study, the study conducted by Varesh et al. on the water vapor changes in different land covers showed that bare lands and rangelands have the least water vapor amounts [34]. The RMSE and land cover map showed that the largest error is for the valleys and wetlands which agrees with the results of Rajeshwari and Mani who demonstrated that the largest error in LST estimation is for vegetation and very humid areas [83].

5. Conclusions

Estimating LST and obtaining temperature information in desert areas is of particular importance, and the use of satellite images and their global coverage has made it possible to measure the temperature of the Earth's surface in desert areas. Summer is very hard and can even be life-threatening. Knowing the temperature situation and its changes in these desert areas can be useful because deserts are still largely unknown. Furthermore, finding a method that improves the accuracy of the first estimate is important in most thermal remote sensing applications. Perhaps the accuracy of even one degree is unimportant for some applications, but it is very important in some cases, such as calculating transpiration evaporation, plant water stress, estimating depth temperature, and determining the location of energy transmission lines. One of the factors affecting the LST estimation accuracy is the amount of AWV.

In this study, LST was estimated using the water vapor image of the MODIS vapor, and its effect on the temperature accuracy was evaluated as well. In addition, the AWV variation rate was examined in different land covers, and the results indicated that the highest to the lowest AWV levels are associated with the mountainous lands, urban areas, agricultural, sand dunes, rangelands, and bare lands, respectively. An examination of

the AWV variations over one year illustrated no significant change within this period. The LST validation was performed by both ground and cross-validation approaches. The results of ground validation showed that bare lands have the lowest error by forming pixels with homogeneous cover, while the highest error in estimating LST is dedicated to regions with sparse vegetation. The results of this validation method estimated the RMSE values corresponding to the improved and general SW algorithms as 1.41 °C and 0.57 °C, respectively, excluding the sparse vegetation regions.

In addition, the cross-validation was performed using the LST images of MODIS satellite, the RMSE statistical index image was evaluated and classified into five groups of less than 2, 2–3, 3–4, 4–5, and greater than 5 °C. The results indicated that the use of the MODIS sensor's water vapor image in the SW algorithm leads to a reduction of about 2.2% in the area of the RMSE group of above 5 °C. Comparing the current results with those of the conducted studies highlights their accuracy. The proposed method in this research is appropriate and easy to use, i.e., there is no need for auxiliary data to determine LST from Landsat 8 satellite images. Hence, the present achievements are helpful for planners and experts at the regional level to acquire knowledge about the AWV and LST status and their relationship with land covers. It can pave the way for managerial decisions to protect the natural and agricultural resources. Future studies shall examine the impact of using MODIS water vapor image on improving the LST accuracy in humid and vegetated regions.

Abbreviations

The following abbreviations are used in this manuscript:

AWV	Atmospheric Water Vapor
BT	Brightness Temperature
EUMETSAT	European Organization for the Exploitation of Meteorological Satellites
FVC	Fractional Vegetation Cover
LSE	Land Surface Emissivity
LST	Land Surface Temperature
MAD	Mean Absolute Differences
MODIS	Moderate Resolution Imaging Spectroradiometer
MSI	Multi-Spectral Instrument
NDVI	Normalized Difference Vegetation Index
NIR	Near Infrared
OLI	Operational Land Imager
RMSE	Root Mean Square Error
SD	Standard Deviation
SW	Split-Window
TIRS	Thermal Infrared Sensor
VZA	Viewing Zenith Angle

References

1. Weng, Q. Thermal infrared remote sensing for urban climate and environmental studies: Methods, applications, and trends. *ISPRS J. Photogramm. Remote Sens.* **2009**, *64*, 335–344. [CrossRef]
2. Bisquert, M.; Sánchez, J.M.; López-Urrea, R.; Caselles, V. Estimating High Resolution Evapotranspiration from Disaggregated Thermal Images. *Remote Sens. Environ.* **2016**, *187*, 423–433. [CrossRef]
3. Koc, C.B.; Osmond, P.; Peters, A. Spatio-temporal patterns in green infrastructure as driver of land surface temperature variability: The case of Sydney. *Int. J. Appl. Earth Obs. Geoinf.* **2019**, *83*, 101903.
4. Guo, J.; Ren, H.; Zheng, Y.; Lu, S.; Dong, J. Evaluation of Land Surface Temperature Retrieval from Landsat 8/TIRS Images before and after Stray Light Correction Using the SURFRAD Dataset. *Remote Sens.* **2020**, *12*, 1023. [CrossRef]
5. Wang, M.; He, G.; Zhang, Z.; Wang, G.; Wang, Z.; Yin, R.; Cao, X. A radiance-based split-window algorithm for land surface temperature retrieval: Theory and application to MODIS data. *Int. J. Appl. Earth Obs. Geoinf.* **2019**, *76*, 204–217. [CrossRef]
6. Hale, R.C.; Gallo, K.P.; Tarpley, D.; Yu, Y. Characterization of variability at in situ locations for calibration/validation of satellite-derived land surface temperature data. *Remote Sens.* **2011**, *2*, 41–50.
7. Ahmed, M.R.; Ghaderpour, E.; Gupta, A.; Dewan, A.; Hassan, Q.K. Opportunities and Challenges of Spaceborne Sensors in Delineating Land Surface Temperature Trends: A Review. *IEEE Sens. J.* **2023**, *23*, 6460–6472. [CrossRef]
8. Ghaderpour, E.; Mazzanti, P.; Scarascia Mugnozza, G.; Bozzano, F. Coherency and phase delay analyses between land cover and climate across Italy via the least-squares wavelet software. *Int. J. Appl. Earth Obs. Geoinf.* **2023**, *118*, 103241. [CrossRef]
9. Shawky, M.; Ahmed, M.R.; Ghaderpour, E.; Gupta, A.; Achari, G.; Dewan, A.; Hassan, Q.K. Remote sensing-derived land surface temperature trends over South Asia. *Ecol. Inform.* **2023**, *74*, 101969. [CrossRef]
10. Dash, P.; Göttsche, F.M.; Olesen, F.; Fischer, H. Retrieval of land surface temperature and emissivity from satellite data: Physics, theoretical limitations and current methods. *J. Indian Soc. Remote Sens.* **2001**, *29*, 23–30. [CrossRef]
11. Ghent, D.; Veal, K.; Trent, T.; Dodd, E.; Sembhi, H.; Remedios, J. A new approach to defining uncertainties for MODIS land surface temperature. *Int. J. Remote Sens.* **2019**, *11*, 1021. [CrossRef]
12. Ren, H.; Dong, J.; Liu, R.; Zheng, Y.; Guo, J.; Chen, S.; Zhao, Y. New hybrid algorithm for land surface temperature retrieval from multiple-band thermal infrared image without atmospheric and emissivity data inputs. *Int. J. Digit. Earth* **2020**, *13*, 1430–1453. [CrossRef]
13. Song, L.; Zhao, Z.; Xu, J.; Liu, S.; Peng, K.; Zhao, K. Improvements in land surface temperature retrieval based on atmospheric water vapor content and atmospheric temperature. *Int. J. Remote Sens.* **2014**, *35*, 4881–4904. [CrossRef]
14. Coll, C.C.; Caselles, J.M.V.; Galve, J.; Valor, E.; Niclos, R.; Sanchez, J.; Rivas, R. Ground Measurements for the Validation of Land Surface Temperatures Derived from AATSR and MODIS Data. *Remote Sens. Environ.* **2005**, *97*, 288–300. [CrossRef]
15. Li, Z.L.; Tang, B.H.; Wu, H.; Ren, H.Z.; Yan, G.J.; Wan, Z.M.; Trigo, I.F.; Sobrino, J.A. Satellite-Derived Land Surface Temperature: Current Status and Perspectives. *Remote Sens. Environ.* **2013**, *131*, 14–37. [CrossRef]
16. Sobrino, J.A.; Li, Z.L.; Stoll, M.P.; Becker, F. Improvement in the split window technique for land surface temperature determination. *IEEE Trans. Geosci. Remote Sens.* **1994**, *32*, 243–253. [CrossRef]
17. Francois, C.; Ottle, C. Atmospheric corrections in the thermal infrared: Global and water vapor dependent split-window algorithm. Application to ATSR and AVHRR data. *IEEE Tran. Geosci. Remote Sens.* **1996**, *34*, 457–471. [CrossRef]
18. Li, Z.L.; Jia, L.; Su, Z.; Wan, Z.; Zhang, R. A new approach for retrieving precipitable water from ATSR2 split-window channel data over land area. *Int. J. Remote Sens.* **2003**, *24*, 5095–5117. [CrossRef]
19. Moradizadeh, M.; Momeni, M.; Saradjian, M.R. Estimation and validation of atmospheric water vapor content using a MODIS NIR band ratio technique based on AIRS water vapor products. *Arab. J. Geosci.* **2014**, *7*, 1891–1897. [CrossRef]
20. Frouin, R.; Deschamps, P.Y.; Lecomte, P. Determination from space of atmospheric total water vapour amounts by differential absorption near 940 nm: Theory and airborne verification. *J. Appl. Meteorol. Climatol.* **1990**, *29*, 460. [CrossRef]
21. Kaufman, Y.J.; Gao, B.C. Remote sensing of water vapor in the near IR from EOS/MODIS. *IEEE Trans. Geosci. Remote Sens.* **1992**, *30*, 871–884. [CrossRef]
22. Schulz, J.; Schluessel, P.; Grassl, H. Water vapor in the atmospheric boundary layer over oceans from SSM/I measurements. *Int. J. Remote Sens.* **1993**, *14*, 2773–2789. [CrossRef]
23. Ottle, C.; Outalha, S.; Francois, C.; Lemaguer, S. Estimation of total atmospheric water vapor content from split-window radiance measurements. *Remote Sens. Environ.* **1997**, *61*, 410–418. [CrossRef]
24. Sobrino, J.A.; Raissouni, N.; Simarro, J.; Nerry, F.; Petitcolin, F. Atmospheric water vapor content over land surfaces derived from AVHRR data: Application to the Iberian Peninsula. *IEEE Trans. Geosci. Remote Sens.* **1999**, *37*, 1425–1434. [CrossRef]
25. Frantz, D.; Stellmes, M.; Hostert, P. A Global MODIS Water Vapor Database for the Operational Atmospheric Correction of Historic and Recent Landsat Imagery. *Int. J. Remote Sens.* **2019**, *11*, 257. [CrossRef]
26. Zhou, J.; Li, J.; Zhang, L.; Hu, D.; Zhan, W. Intercomparison of methods for estimating land surface temperature from a Landsat-5 TM image in an arid region with low water vapour in the atmosphere. *Int. J. Remote Sens.* **2012**, *33*, 2582–2602. [CrossRef]
27. Zhang, Z.; He, G.; Wang, M.; Long, T.; Wang, G.; Zhang, X.; Jiao, W. Towards an operational method for land surface temperature retrieval from Landsat 8 data. *Remote Sens. Lett.* **2016**, *7*, 279–288. [CrossRef]

28. Wang, F.; Qin, Z.; Song, C.; Tu, L.; Karnieli, A.; Zhao, S. An improved mono-window algorithm for land surface temperature retrieval from Landsat 8 thermal infrared sensor data. *Remote Sens.* **2015**, *7*, 4268–4289. [CrossRef]

29. Cristóbal, J.; Jiménez-Muñoz, J.; Prakash, A.; Mattar, C.; Skoković, D.; J, S. An improved single-channel method to retrieve land surface temperature from the Landsat-8 Thermal Band. *Remote Sens.* **2018**, *10*, 431. [CrossRef]

30. Gao, B.C.; Kaufman, Y.J. Water vapor retrievals using Moderate Resolution Imaging Spectroradiometer (MODIS) near-infrared channels. *J. Geophys. Res. Atmos.* **2003**, *108*, 4389. [CrossRef]

31. Kern, A.; Bartholy, J.; Borbás, É.E.; Barcza, Z.; Pongrácz, R.; C, F. Estimation of vertically integrated water vapor in Hungary using MODIS imagery. *Adv. Space Res.* **2008**, *41*, 1933–1945. [CrossRef]

32. Sobrino, J.A.; Jiménez-Muñoz, J.C.; Mattar, C.; Sòria, G. Evaluation of Terra/MODIS atmospheric profiles product (MOD07) over the Iberian Peninsula: A comparison with radiosonde stations. *Int. J. Digit. Earth* **2015**, *8*, 771–783. [CrossRef]

33. Albert, P.; Bennartz, R.; Preusker, R.; Leinweber, R.; J, F. Remote sensing of atmospheric water vapor using the moderate resolution imaging spectroradiometer. *J. Atmos. Ocean. Technol.* **2005**, *22*, 309–314. [CrossRef]

34. Varamesh, S.; Hosseini, S.M.; Rahimzadegan, M. Estimation of atmospheric water vapor using MODIS data 1. (case study: Golestan province of Iran). *J. Mater. Environ. Sci.* **2017**, *8*, 1690–1695.

35. Vaquero-Martínez, J.; Antón, M.; de Galisteo, J.P.O.; Cachorro, V.E.; Costa, M.J.; Román, R.; Bennouna, Y.S. Validation of MODIS integrated water vapor product against reference GPS data at the Iberian Peninsula. *Int. J. Appl. Earth Obs. Geoinf.* **2017**, *63*, 214–221. [CrossRef]

36. Mancino, G.; Ferrara, A.; Padula, A.; Nolè, A. Cross-Comparison between Landsat 8 (OLI) and Landsat 7 (ETM+) Derived Vegetation Indices in a Mediterranean Environment. *Remote Sens.* **2020**, *12*, 291. [CrossRef]

37. Neinavaz, E.; Skidmore, A.K.; Darvishzadeh, R. Effects of prediction accuracy of the proportion of vegetation cover on land surface emissivity and temperature using the NDVI threshold method. *Int. J. Appl. Earth Obs. Geoinf.* **2020**, *85*, 101984. [CrossRef]

38. Frey, R.A.; Ackerman, S.A.; Liu, Y.; Strabala, K.I.; Zhang, H.; Key, J.R.; Wang, X. Cloud detection with MODIS. Part I: Improvements in the MODIS cloud mask for collection 5. *J. Atmos. Ocean. Technol.* **2008**, *25*, 1057–1072. [CrossRef]

39. Wan, Z.; Zhang, Y.; Zhang, Q.; Li, Z.L. Validation of the land-surface temperature products retrieved from Terra Moderate Resolution Imaging Spectroradiometer data. *Remote Sens. Environ.* **2002**, *83*, 163–180. [CrossRef]

40. Wan, Z.M.; Zhang, Y.L.; Zhang, Q.C.; Li, Z.L. Quality assessment and validation of the MODIS global land surface temperature. *Remote Sens.* **2004**, *25*, 261–274. [CrossRef]

41. Wan, Z. New refinements and validation of the Collection-6 MODIS land-surface temperature/emissivity products. *Remote Sens. Environ.* **2014**, *140*, 36–45. [CrossRef]

42. Lu, L.; Zhang, T.; Wang, T.; Zhou, X. Evaluation of Collection-6 MODIS Land Surface Temperature Product Using Multi-Year Ground Measurements in an Arid Area of Northwest China. *Remote Sens.* **2018**, *10*, 1852. [CrossRef]

43. Yang, J.; Duan, S.B.; Zhang, X.; Wu, P.; Huang, C.; Leng, P.; Gao, M. Evaluation of Seven Atmospheric Profiles from Reanalysis and Satellite-Derived Products: Implication for Single-Channel Land Surface Temperature Retrieval. *Remote Sens.* **2020**, *12*, 791. [CrossRef]

44. Akbari, E.; Boloorani, A.D.; Samany, N.N.; Hamzeh, S.; Soufizadeh, S.; Pignatti, S. Crop Mapping Using Random Forest and Particle Swarm Optimization Based on Multi-Temporal Sentinel-2. *Remote Sens.* **2020**, *12*, 1449. [CrossRef]

45. Drusch, M.; Bello, U.D.; Carlier, S.; Colin, O.; Fernandez, V.; Gascon, F.; Hoersch, B.; Isola, C.; Laberinti, P.; Martimort, P.; et al. Sentinel-2: ESA's optical high-resolution mission for (GMES) operational services. *Remote Sens. Environ.* **2012**, *120*, 25–36. [CrossRef]

46. Wan, Z.; Dozier, J. A generalized split-window algorithm for retrieving land-surface temperature from space. *IEEE Trans. Geosci. Remote Sens.* **1996**, *34*, 892–905.

47. Qin, Z.; Berliner, P.; Karnieli, A. A mono-window algorithm for retrieving land surface temperature from Landsat TM data and its application to the Israel- Egypt border region. *Int. J. Remote Sens.* **2001**, *22*, 3719–3746. [CrossRef]

48. Jimenez-Munoz, J.C.; Sobrino, J.A. A generalized single-channel method for retrieving land surface temperature from remote sensing data. *J. Geophys. Res. Atmos.* **2003**, *108*, 4688. [CrossRef]

49. Jin, M.; Li, J.; Wang, C.; Shang, R. A Practical Split-Window Algorithm for Retrieving Land Surface Temperature from Landsat-8 Data and a Case Study of an Urban Area in China. *Int. J. Remote Sens.* **2015**, *7*, 4371–4390. [CrossRef]

50. McMillin, L.M. Estimation of sea surface temperatures from two infrared window measurements with different absorption. *J. Geophys. Res.* **1975**, *80*, 5113–5117. [CrossRef]

51. Jiang, G.M.; Zhou, W.; Liu, R. Development of split-window algorithm for land surface temperature estimation from the VIRR/FY-3A measurements. *IEEE Geosci. Remote Sens. Lett.* **2013**, *10*, 952–956. [CrossRef]

52. Franc, G.B.; Cracknell, A.P. Retrieval of land and sea surface temperature using NOAA-11 AVHRR data in north-eastern Brazil. *Int. J. Remote Sens.* **1994**, *15*, 1695–1712. [CrossRef]

53. Sun, D.; Pinker, R.T. Estimation of land surface temperature from a Geostationary Operational Environmental Satellite (GOES-8). *J. Geophys. Res. Atmos.* **2003**, *108*, 4326. [CrossRef]

54. Ren, H.; Ye, X.; Liu, R.; Dong, J.; Qin, Q. Improving land surface temperature and emissivity retrieval from the Chinese Gaofen-5 satellite using a hybrid algorithm. *IEEE Trans. Geosci. Remote Sens.* **2018**, *56*, 1080–1090. [CrossRef]

55. Jiménez-Muñoz, J.C.; Sobrino, J.A.; Jiménez, D.; Mattar, C.; Cristóbal, J. Land Surface Temperature Retrieval Methods from Landsat-8 Thermal Infrared Sensor Data. *IEEE Geosci. Remote Sens. Lett.* **2014**, *11*, 1840–1843. [CrossRef]

56. García-Santos, V.; Cuxart, J.; Martínez-Villagrasa, D.; Jiménez, M.A.; Simó, G. Comparison of Three Methods for Estimating Land Surface Temperature from Landsat 8-TIRS Sensor Data. *Int. J. Remote Sens.* **2018**, *10*, 1450. [CrossRef]

57. Sobrino, J.A.; Raissouni, N. Toward remote sensing methods for land cover dynamic monitoring: Application to Morocco. *Remote Sens.* **2000**, *21*, 353–366. [CrossRef]

58. Guha, S.; Govil, H.; Dey, A.; Gill, N. Analytical study of land surface temperature with NDVI and NDBI using Landsat 8 OLI and TIRS data in Florence and Naples city, Italy. *Eur. J. Remote Sens.* **2018**, *51*, 667–678. [CrossRef]

59. Dymond, J.R.; Stephens, P.R.; Newsome, P.F.; Wilde, R.H. Percentage vegetation cover of a degrading rangeland from SPOT. *Int. J. Remote Sens.* **1992**, *13*, 1999–2007. [CrossRef]

60. Vlassova, L.; Perez-Cabello, F.; Nieto, H.; Martín, P.; Riaño, D.; De La Riva, J. Assessment of methods for land surface temperature retrieval from Landsat-5 TM images applicable to multiscale tree-grass ecosystem modeling. *Remote Sens.* **2014**, *6*, 4345–4368. [CrossRef]

61. Arabi Aliabad, F.; Ghafarian Malmiri, H.; Sarsangi, A.; Sekertekin, A.; Ghaderpour, E. Identifying and Monitoring Gardens in Urban Areas Using Aerial and Satellite Imagery. *Remote Sens.* **2023**, *15*, 4053. [CrossRef]

62. Román, R.; Antón, M.; Cachorro, V.; Loyola, D.; Ortiz de Galisteo, J.; de Frutos, A.; Romero-Campos, P. Comparison of total water vapor column from GOME-2 on MetOp-A against ground-based GPS measurements at the Iberian Peninsula. *Sci. Tot. Environ.* **2015**, *533*, 317–328. [CrossRef] [PubMed]

63. Vaquero-Martínez, J.; Antón, M.; de Galisteo, J.P.O.; Román, R.; Cachorro, V.E. Water vapor radiative effects on short-wave radiation in Spain. *Atmos. Res.* **2018**, *205*, 18–25. [CrossRef]

64. Sobrino, J.A.; ElKharraz, J.; Li, Z.L. Surface temperature and water vapor retrieval from MODIS data. *Int. J. Remote Sens.* **2003**, *24*, 5161–5182. [CrossRef]

65. Chen, M.; Su, W.; Li, L.; Yue, A.; Li, H. A comparison of Pixel-based and Object-oriented Knowledge-based Classification Methods Using SPOT5 Imagery. *WSEAS Trans. Inf. Sci. Appl.* **2010**, *6*, 477–489.

66. Mather, P.M.; Koch, M. *Computer Processing of Remotely Sensed Images: An Introduction*, 4th ed.; Wiley: Hoboken, NJ, USA, 2010; p. 464.

67. Sekertekin, A.; Bonafoni, S. Land Surface Temperature Retrieval from Landsat 5, 7, and 8 over Rural Areas: Assessment of Different Retrieval Algorithms and Emissivity Models and Toolbox Implementation. *Remote Sens.* **2020**, *12*, 294. [CrossRef]

68. Peng, W.; Zhoua, J.; Wena, L.; Xuea, S.; Dong, L. Land surface temperature and its impact factors in Western Sichuan Plateau, China. *Geocarto Int.* **2017**, *32*, 919–934. [CrossRef]

69. Jaber, S.M.; Abu-Allaban, M.M. MODIS-based land surface temperature for climate variability and change research: The tale of a typical semi-arid to arid environment. *Eur. J. Remote Sens.* **2020**, *53*, 81–90. [CrossRef]

70. Yu, X.; Guo, X.; Wu, Z. Land surface temperature retrieval from Landsat 8 TIRS-comparison between radiative transfer equation-based method, split window algorithm, and single channel method. *Remote Sens.* **2014**, *6*, 9829–9852. [CrossRef]

71. Malakar, N.K.; Hulley, G.C.; Hook, S.J.; Laraby, K.; Cook, M.; Schott, J.R. An operational land surface temperature product for Landsat thermal data: Methodology and validation. *IEEE Trans. Geosci. Remote Sens.* **2018**, *56*, 5717–5735. [CrossRef]

72. Wan, Z.; Li, Z.L. Radiance-based validation of the V5 MODIS land-surface temperature product. *Remote Sens.* **2008**, *29*, 5373–5395. [CrossRef]

73. Coll, C.; Caselles, V.; Valor, E.; Niclòs, R. Comparison between different sources of atmospheric profiles for land surface temperature retrieval from single channel thermal infrared data. *Remote Sens. Environ.* **2012**, *117*, 199–210. [CrossRef]

74. Sánchez, J.M.; Galve, J.M.; González-Piqueras, J.; López-Urrea, R.; Niclòs, R.; Calera, A. Monitoring 10-m LST from the Combination MODIS/Sentinel-2, Validation in a High Contrast Semi-Arid Agroecosystem. *Remote Sens.* **2020**, *12*, 1453. [CrossRef]

75. Qian, Y.G.; Li, Z.L.; Nerry, F. Evaluation of land surface temperature and emissivities retrieved from MSG-SEVIRI data with MODIS land surface temperature and emissivity products. *Int. J. Remote Sens.* **2013**, *34*, 3140–3152. [CrossRef]

76. Kuenzer, C.; Dech, S. *Thermal Infrared Remote Sensing, Sensors, Methods, Applications*; Springer: Berlin/Heidelberg, Germany, 2013; p. 537. [CrossRef]

77. Duan, S.B.; Li, Z.L.; Li, H.; Göttsche, F.M.; Wu, H.; Zhao, W.; Leng, P.; Zhang, X.; Coll, C. Validation of Collection 6 MODIS land surface temperature product using in situ measurements. *Remote Sens. Environ.* **2019**, *225*, 16–29. [CrossRef]

78. Yu, P.; Zhao, T.; Shi, J.; Ran, Y.; Jia, L.; Ji, D.; Xue, H. Global spatiotemporally continuous MODIS land surface temperature dataset. *Sci. Data* **2022**, *9*, 143. [CrossRef] [PubMed]

79. Niclòs, R.; Galve, J.M.; Valiente, J.A.; Estrela, M.J.; Coll, C. Accuracy assessment of land surface temperature retrievals from MSG2-SEVIRI data. *Remote Sens. Environ.* **2011**, *115*, 2126–2140. [CrossRef]

80. Marques da Silva, J.; Damásio, C.; Sousa, A.; Bugalho, L.; Pessanha, L.; Quaresma, P. Agriculture pest and disease risk maps considering MSG satellite data and land surface temperature. *Int. J. Appl. Earth Obs. Geoinf.* **2015**, *38*, 40–50. [CrossRef]

81. Ren, H.; Du, C.; Liu, R.; Qin, Q.; Yan, G.; Li, Z.L.; Meng, J. Atmospheric water vapor retrieval from Landsat 8 thermal infrared images. *J. Geophys. Res. Atmos.* **2015**, *120*, 1723–1738. [CrossRef]

82. Tardy, B.; Rivalland, V.; Huc, M.; Hagolle, O.; Marcq, S.; Boulet, G. A software tool for atmospheric correction and surface temperature estimation of Landsat infrared thermal data. *Remote Sens.* **2016**, *8*, 696. [CrossRef]

83. Rajeshwari, A.; Mani, N.D. Estimation of Land Surface Temperature of Dindigul District Using Landsat 8 Data. *Int. J. Res. Eng. Technol.* **2014**, *3*, 122–126.